ELSEVIER

Ocean Modelling 4 (2002) 269–289

Ocean Modelling

www.elsevier.com/locate/omodol

Alleviating the Garden Sprinkler Effect in wind wave models ☆

Hendrik L. Tolman *

SAIC-GSO at NOAA/NCEP/EMC Ocean Modeling Branch, 5200 Auth Road, Room 209, Camp Springs, MD 20746, USA

Abstract

In ocean wave models, swell propagation at coarse spectral resolution leads to the disintegration of continuous swell fields into discrete swell fields. This process is known as the Garden Sprinkler Effect (GSE). An existing solution to the GSE consists of adding a diffusion tensor to the propagation equation. Although this diffusion method has been proven successful, it is prohibitively expensive for models with high spatial resolution. Two alternatives are presented here. The first is an averaging method. It shares characteristics with the diffusion method, but is much cheaper for high resolution models. The second method consists of adding divergence to the advection field. This divergence method is shown to be accurate for idealized conditions, and requires less tuning, but is still too expensive to replace the other methods in practical conditions. It is therefore suggested to replace the diffusion method with an averaging method in operational models, and to investigate the divergence method further.

Keywords: Wind waves; Garden Sprinkler Effect; Numerical modelling

1. Introduction

Ocean wave models solve some form of the spectral energy or action balance equation, such as

$$\frac{\mathrm{D}F}{\mathrm{D}t} = S, \tag{1}$$

where F is a wind wave spectrum, and S represents source terms for spectral wave energy due to the influence of wind, wave breaking ('whitecapping'), nonlinear interactions, and additional (mostly shallow-water) processes. In the spectral description used in Eq. (1), the spectrum F and

☆ OMB contribution Nr. 211.

* Tel.: +1-301-763-8000x7253; fax: +1-301-763-8545.
E-mail address: hendrik.tolman@noaa.gov (H.L. Tolman).

1463-5003/02/$ - see front matter
PII: S1463-5003(02)00004-5

source term S are functions of two parameters describing spectral space. Conventionally, these have been the spectral frequency f and direction θ. Although alternative descriptions have been used, the differences are immaterial for the present study. The spectrum is furthermore a slowly varying function of space $\vec{x}$ and time t (compared to the length and period of individual waves)

$$F = F(f, \theta; \vec{x}, t), \quad S = S(f, \theta; \vec{x}, t). \tag{2}$$

In a conventional numerical wave model, spectral space (f, θ) and physical space $\vec{x}$ are discretized, while the solution is propagated with discrete time steps Δt. The need to discretize in four dimensions makes it difficult to attain resolution and economy at the same time. In state-of-the-art wave models like WAM (WAMDIG, 1988; Komen et al., 1994), WAVEWATCH III (Tolman and Chalikov, 1996; Tolman, 1999), and SWAN (Booij et al., 1999; Ris et al., 1999), a typical spectral resolution is 24 directions with $\Delta\theta = 15°$, and a logarithmic frequency distribution

$$f_{i+1} = \gamma f_i, \tag{3}$$

where i is the discrete grid counter in f-space, and typically $\gamma = 1.10$. Better resolutions have been used, but the parameterization of nonlinear interactions as used in these models (the Discrete Interaction Approximation, DIA, Hasselmann et al., 1985), appears best suited for such a resolution. Furthermore, this resolution appears sufficient to adequately describe (local) wave growth (e.g., Tolman, 1992). With this spectral resolution, spatial resolution appears to have been mostly dictated by economics, and to optimally use nominal resolutions of modelled wind fields employed to drive these models.

Whereas the above described common resolutions appear generally adequate in conditions of active wave generation, problems occur when active wave generation stops, and wind seas become swell. Such swells travel across the ocean, virtually without interacting with other wave groups (e.g., Snodgrass et al., 1966). Due to continuous dispersion of swell energy with different frequencies and directions, a swell field covers an increasingly large area. In numerical models, however, the spectral frequency and direction are not continuous but discretized. Discrete swell fields therefore travel in discrete directions with discrete speeds (i.e., discrete frequencies). If the spectral resolutions are inadequate, this will result in a spurious disintegration of the continuous swell field into discrete swell fields. This numerical problem is generally known as the Garden Sprinkler Effect (GSE).

The GSE and possible solutions to it have been discussed in great detail by Booij and Holthuijsen (1987, henceforth denoted as BH87). To illustrate the effects of the GSE, results of a test case similar to theirs are presented here. In this test, propagation in deep water in a Cartesian (x, y) space is considered. Eq. (1) then reduces to

$$\frac{\partial F}{\partial t} + c_x \frac{\partial F}{\partial x} + c_y \frac{\partial F}{\partial y} = 0, \tag{4}$$

where c_x and c_y are the group velocity components in the respective directions.

In an area of 4500×3500 km^2, discretized with $\Delta x = \Delta y = 100$ km, an initial wave field is placed at 500 km from the lower and left side (point $(0, 0)$ in all figures). The initial wave field has a significant wave height $H_s = 2.5$ m. The mean direction $\theta_m = 30°$, and the directional energy distribution is of the $\cos^2(\theta - \theta_m)$ type. The mean frequency $f_m = 0.1$ Hz, and the distribution of energy in frequency space is Gaussian with a spread of 0.01 Hz. The distribution of wave energy in

physical space is also Gaussian with a spread of 150 km. The model is run for five days to propagate the swell field to the top and right edges of the area. Numerical results are obtained using the ULTIMATE QUICKEST (UQ) scheme of Leonard (1979, 1991). Calculations are performed with a test version of WAVEWATCH III. From the perspective of the present study, the only relevant differences between the test version of this model and its presently distributed version (Tolman, 1999) is the option to run the model on Cartesian instead of spherical spatial grids, and the inclusion of new GSE alleviation methods as presented in the present study.

Fig. 1(a) shows the initial conditions and final wave heights obtained with the conventional spectral resolution $\Delta\theta = 15°$ and $\gamma = 1.10$. Fig. 1(b) shows the corresponding near-exact results as obtained with a highly increased resolution of $\Delta\theta = 2.5°$, $\gamma = \sqrt{1.10}$ and $\Delta x = \Delta y = 25$ km. Whereas the 'exact' solution shows the expected continuous swell dispersion, the conventional model results show a clear GSE. Particularly, the discrete swell fields for individual discrete directions are obvious. In frequency space discrete swell fields travel at different speeds in the same direction. Because no clear separation of fields is obvious in the propagation direction, the frequency resolution $\gamma = 1.10$ is apparently sufficient for the propagation distances and spatial extent of the initial distribution considered here.

As already mentioned above, BH87 present solutions to the GSE. The obvious solution is to increase spectral, in particular directional, resolutions. The required resolution, however ($\Delta\theta \ll 5°$), is not economically feasible in operational models. Alternatively, BH87 present a modified propagation equation:

$$\frac{\partial F}{\partial t} + \frac{\partial}{\partial x}\left[c_x F - D_{xx}\frac{\partial F}{\partial x}\right] + \frac{\partial}{\partial y}\left[c_y F - D_{yy}\frac{\partial F}{\partial y}\right] - 2D_{xy}\frac{\partial^2 F}{\partial x \partial y} = 0, \tag{5}$$

$$D_{xx} = D_{ss}\cos^2\theta + D_{nn}\sin^2\theta, \tag{6}$$

$$D_{yy} = D_{ss}\sin^2\theta + D_{nn}\cos^2\theta, \tag{7}$$

$$D_{xy} = (D_{ss} - D_{nn})\cos\theta\sin\theta, \tag{8}$$

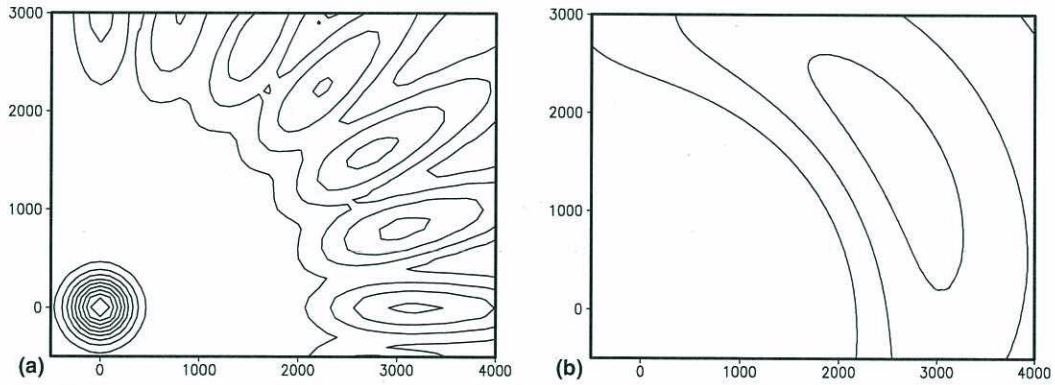

Fig. 1. Significant wave height (H_s) for simple GSE test as described in text. (a) Initial conditions near (0, 0) with contours at 0.25 m intervals, and model results after 5 days with contours at 0.10 m intervals for conventional spectral resolution with $\Delta\theta = 15°$ and $\gamma = 1.10$. (b) Near-exact results obtained with increased spatial and spectral resolution. Axes in km.

$$D_{ss} = (\Delta c_g)^2 T_s/12, \tag{9}$$

$$D_{nn} = (c_g \Delta\theta)^2 T_s/12, \tag{10}$$

where D_{ss} is the diffusion coefficient in the propagation direction of the discrete wave component, and D_{nn} is the diffusion coefficient along the crest of the discrete wave component. D_{xx}, D_{yy} and D_{xy} are the corresponding components of the diffusion tensor along the axes of the spatial grid. c_g is the group velocity with which the wave energy propagates in the direction θ, and Δc_g is the discrete increment in c_g corresponding to Δf. T_s is the time elapsed since the generation of the swell, or the 'swell age'. Compared to Eq. (4), Eq. (5) adds a diffusion tensor. This diffusion explicitly models sub-grid dispersion.

Formally, the evaluation of the diffusion requires the evaluation of $T_s(f,\theta)$ with a set of equations similar to Eqs. (5)–(10) (see BH87 for details). This will obviously impact memory requirements and run times of models seriously. It will also make evaluation of the stability of the numerical scheme (see below) more complicated. BH87 suggest simplifying this approach by using a single representative swell age T_s. This then becomes a tunable parameter, which needs to be estimated for each model application separately based upon the travel time of typical swells across the model domain. Figs. 2(a) and (b) show model results for the test case after 5 days for $T_s = 2$ and 4 days, respectively. Results obtained with $T_s = 2$ days (Fig. 2(a)) show a less pronounced, but still obvious GSE. Results obtained with $T_s = 4$ days (Fig. 2(b)) show a nearly complete removal of the GSE. A further increase of T_s to 5 days would remove the last trace of the GSE (see similar test in Tolman, 2001).

From the above tests, it is obvious that the BH87 solution for the GSE is effective. Operational WAVEWATCH III wave models as run at the National Centers for Environmental Prediction (NCEP), have shown both the need for GSE removal, and the success of the BH87 in doing so for practical conditions. This will be illustrated in the following sections. However, this practical experience has also illustrated a problem with the BH87 solution. For simple advection as in Eq. (4), the maximum allowed numerical time step $\Delta t_{max,a}$ for explicit numerical schemes scales with the grid increment

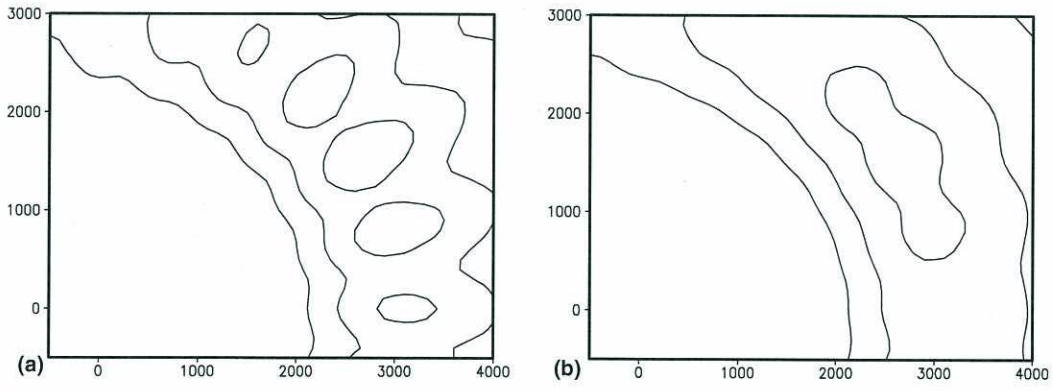

Fig. 2. Like panel (b) of Fig. 1 for UQ scheme with BH87 GSE correction and $T_s = 2$ days (panel (a)) or $T_s = 4$ days (panel (b)).

$$\Delta t_{\max,a} \propto \frac{\Delta x}{c_g}. \tag{11}$$

For explicit schemes for the diffusion as in Eq. (5), however, the maximum time step $\Delta t_{\max,d}$ scales with the diffusion coefficient (and therefore with T_s^{-1}) and the square grid size (Tolman, 1999, p. 33)

$$\Delta t_{\max,d} \propto \frac{(\Delta x)^2}{(c_g \Delta\theta)^2 T_s}. \tag{12}$$

Thus, for increasing spatial resolution (decreasing Δx), the diffusion will eventually dictate the numerical time step for Eq. (5), or alternatively, the time step will limit the maximum T_s attainable.

For NCEP's operational global wave model (Chen et al., 1999) with a spatial resolution of about 100 km, T_s was set to 4 days. This choice is based on the test results of Tolman (1995). With the given spatial resolution, this choice of T_s does not influence the required time step, and the GSE correction increases the computing time for the model by a modest 15%. For NCEP's regional models, however, the spatial resolution is typically 25 km. To obtain necessary swell ages of about 3 days (based upon practical experience with the North Atlantic Hurricane model), the propagation time step of the model needs to be reduced by a factor of 3, compared to a model with advection only. This increases the necessary computational time by about 75%. Even though this increase is manageable in NCEP's operational environment, it is sufficiently large to justify the start of a search for alternative GSE alleviation methods. Furthermore, future wave model implementations are expected to require even higher resolution, further compounding the present negative effect of the BH87 approach on overall model run times.

Methods other than BH87 have been used or suggested to cope with the GSE. Some models rely on numerical diffusion inherent to the spatial propagation scheme to mask the GSE. Such numerical diffusion, however, by definition has major axes associated with the physical (x, y) grid. Eq. (5), on the other hand, indicates that the major axes of the diffusion need to be lined up with the spectral direction θ. Consequently, there is little hope for numerical diffusion in physical space to effectively remove the GSE. Nevertheless diffusive propagation schemes do mask the GSE to some extend. Accurate schemes like the UQ scheme used in WAVEWATCH III tend to highlight the GSE.

Another method is presented by Lavrenov and Onvlee (1995). Instead of adding diffusion in physical space, they add averaging in θ-space. Their test case indicates some success in removing the GSE, but is less taxing than the present test due to the much larger spatial scale of the initial condition. The directional averaging for a given discrete location and frequency is defined as

$$F^{n+1}(\theta_j) = \epsilon[F^n(\theta_{j-1}) + F^n(\theta_{j+1})] + (1 - 2\epsilon)F^n(\theta_j), \tag{13}$$

where n and j are discrete counters in time and direction, and ϵ is a small number scaling with $c_g \Delta t$. Such an averaging has the disadvantage that some, albeit little, energy is rapidly spread over all directions, and will hence spread through the entire model domain. Conversely, the BH87 approach retains all energy in the dominant propagation direction, spreading energy in physical space with a process that still is dominated by the mean advection. Such a method is much more selective in spreading energy throughout a model. Therefore, GSE solutions confined to physical space appear preferable.

In the present study, two such GSE alleviation methods will be presented. The first uses a spatial averaging technique, and is discussed in Section 2. The second adds divergence to the advection velocity, and is discussed in Section 3. The effectiveness of both methods is assessed using the test case of Fig. 1. Impact of the GSE in practical conditions, as well as the corresponding success of GSE alleviation methods, is illustrated in Section 4. A final discussion and conclusions are presented in Sections 5 and 6.

2. Spatial averaging

As discussed above, the GSE occurs due to the inability of typical Eulerian propagation schemes to describe spectral dispersion within discrete spectral bins. A simple solution would be to try and account for the variability of the advection velocity $(\Delta c_g, \Delta\theta)$ within the numerical scheme by averaging. This approach, however, is doomed to fail. In general, a Eulerian scheme for one-dimensional propagation can be written as

$$F_l^{n+1} = \sum_{m=-M}^{M} a_m F_{l+m}^n, \tag{14}$$

where l is the discrete grid counter, m is a secondary grid counter in the same space, and M represents the so-called 'stencil width' of the numerical scheme. The coefficients a_m are a function of the advection velocity, grid spacing and time step. If the advection velocity is allowed to vary to describe variability within the spectral bin, this only affects the coefficients a_m in Eq. (14). The subsequent averaging will also only affect the coefficients. In a linear perturbation approach, the coefficients after averaging will simply return the coefficient values of the mean of the spectral bin. Hence, straightforward averaging of an Eulerian scheme to the first order has no influence on the scheme, and can therefore not alleviate the GSE.

In a Lagrangian, or semi-Lagrangian approach, a direct averaging method will be similarly unsuccessful. In such a scheme, the spectral density at the next time step is estimated from the energy density at the previous time step with spatial offset $-\vec{c}_g\Delta t$ (○ in Fig. 3). The energy density at this target point is estimated using some kind of interpolation from the discrete spatial grid.

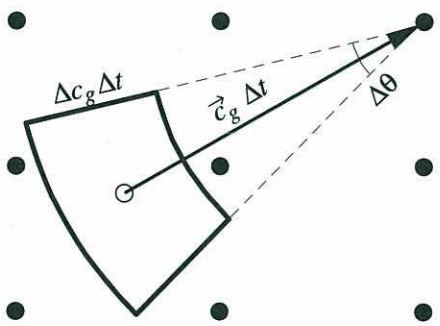

Fig. 3. The GSE from a Lagrangian or semi-Lagrangian perspective: •, discrete spatial grid points; ○, 'target' point of scheme.

This interpolation can be written in a general two-dimensional version of Eq. (14). If the dispersion within the spectral grid box is considered, the target point is replaced by a target area around the target point, defined by $\Delta c_g \Delta t$ and $\Delta\theta$. Averaging of the interpolation over the area will again simply return the mean value (in a linearized approach), and hence will not avoid the GSE. This is particularly obvious in the case where the target area in Fig. 3 is completely surrounded by four grid points. Only in cases where the averaging results in the inclusion of additional spatial grid points, some residual effect of averaging will occur.

There appears to be a paradox in Fig. 3; the GSE occurs because spatial averaging is not performed, yet including spatial averaging within the numerical Eulerian or Lagrangian scheme does not help. A simple solution to this apparent paradox is to separate the averaging from the propagation scheme in a separate fractional step. In one of the steps, an arbitrary numerical scheme is used to propagate the solution. In the other step the averaging is performed. If the averaging is performed separately, the averaging needs to be done relative to the grid points (•) rather than target points (○). Using a simple linearization, the extent of the averaging in the propagation ($\vec{e}_s$) and normal ($\vec{e}_n$) directions become

$$\pm\alpha_s \Delta c_g \Delta t \vec{e}_s, \quad \pm\alpha_n c_g \Delta\theta \Delta t \vec{e}_n, \tag{15}$$

where α_s and α_n are constants. Ideally, $\alpha_s = \alpha_n = 0.5$. Varying these constants leaves room for some tuning of such a GSE alleviation method. Note that this kind of averaging with dominant directions $\vec{e}_s$ and $\vec{e}_n$ is similar to the BH87 diffusion method, that uses the same main directions. The averaging method, however, never influences the time step, because it is completely separated from the actual propagation. Moreover, if explicit schemes are used with typically $c_g \Delta t/\Delta x < 1$, it is obvious that the averaging over the area as defined in (15) will generally require information at directly neighboring spatial grid points only.

Clearly, the resulting scheme depends on the averaging scheme used. Considering the similarity with the tensor-like solution of BH87, it appears important to use a full nine-point stencil around the grid points, rather than stencils along the main spatial grid axes only. This naturally lends itself to an 'octant type' interpolation to get the field values at the edges of the averaging area. This is illustrated in Fig. 4. The hatched area in this figure represents the averaging area. Energies F at the corner points of this area are obtained by linear interpolation from F at the central point

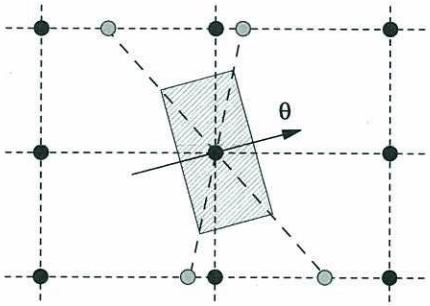

Fig. 4. Graphical depiction of spatial averaging technique used here. Solid circles and dotted lines represent the spatial grid. Hatched area represent averaging area to be considered. Corner point values are obtained from central grid point and gray points. The latter values are obtained by interpolation from adjacent grid points.

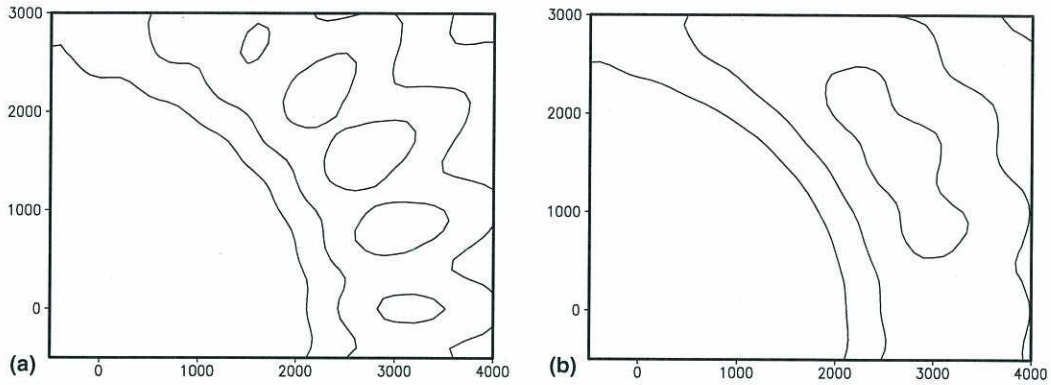

Fig. 5. Like panel (b) of Fig. 1 for UQ scheme with averaging technique and $\alpha_n = \alpha_s = 0.75$ (panel (a)) or $\alpha_n = \alpha_s = 1.50$ (panel (b)).

and F at the border of the stencil (gray points). The values for F at the latter points are obtained by linear interpolation from the adjacent grid points. Details of the averaging can be found in Appendix A.

Fig. 5 shows test results after 5 days for the UQ scheme augmented with spatial averaging for several values of α_s and α_n. With this choice of tuning parameters, the results are virtually identical to those of the BH87 solution as presented in Fig. 2. Results obtained with $\alpha_s = \alpha_n = 0.75$ (Fig. 5(a)) show a less pronounced, but still obvious GSE. Results obtained with $\alpha_s = \alpha_n = 1.50$ (Fig. 5(b)) show a nearly complete removal of the GSE. Setting $\alpha_s = \alpha_n = 2.00$ would remove the last trace of the GSE (see comparable test in Tolman, 2001). Note that even with the relatively large values of α used here, the averaging area is still well within the nine-point stencil.

3. Divergent advection

With the existing solution of BH87, and the general origin of the GSE, averaging techniques as described in the previous section form a logical approach to alleviating the GSE. In the previous section, Eq. (4) was also shown to not reproduce dispersion within the spectral bin by means of direct averaging of the equation. However, if this equation is written in the more general flux form

$$\frac{\partial F}{\partial t} + \frac{\partial c_x F}{\partial x} + \frac{\partial c_y F}{\partial y} = 0 \tag{16}$$

it is clear that spatial dispersion of energy F can be achieved by adding divergence to the normally homogeneous advection field $\vec{c}_g = (c_x, c_y)$. Such an approach is not only possible, but also physically sound. Consider again, that the energy at a given bin (f_i, θ_j) in fact contains wave energy in a band $(\Delta f, \Delta\theta)$. After a wave field has propagated for some time the spatial dispersion pattern of the energy for this bin will reflect the fact that propagation of energy in a spectral band is considered. Wave energy to the left of the discrete propagation direction in fact travels more in that direction than in the mean direction for the bin, etc. Thus, the actual advection pattern is not homogeneous, but looks as illustrated in Fig. 6.

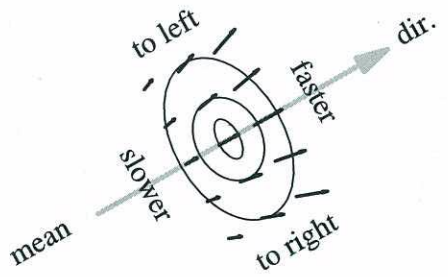

Fig. 6. Graphical depiction of actual dispersion pattern of discrete wave field.

To establish a dispersion pattern as in Fig. 6, the spatial extent and location of individual swell fields needs to be evaluated. In principle, additional evolution equations for location and size of discrete swell fields could be established. Although perhaps cumbersome to evaluate, such equations will require relatively little additional computational effort, because only a small number of parameters need to be evaluated per discrete wave field. In contrast, the evolution equation for T_s in BH87 is required for each discrete spectral and spatial bin. From a modelling perspective, a direct and instantaneous method to evaluate the necessary divergence appears more simple and, therefore, preferable for initial tests.

A simple algorithm can be constructed as follows. First the center of a discrete swell field for the spectral bin (f_i, θ_j) is defined by the location of the maximum energy density $F(f_j, \theta_j)_{\max}$. Secondly, the extent of the swell field in the propagation (θ) direction, $r_{s,\max}$, and in the normal direction, $r_{n,\max}$ are estimated by evaluating whether

$$F(f_j, \theta_j; x, y) < \beta_0 F(f_j, \theta_j)_{\max}. \tag{17}$$

Ideally, $\beta_0 = 0$. From general numerical considerations, β_0 should be a small number of the order 0.01–0.1. Assuming a linear correction of advection speed and direction with the actual propagation (r_s) and normal (r_n) distances to the center of the discrete swell field, the advection speed c_g and direction θ, relative to their original bin-mean values $c_{g,0}$ and θ_0 become

$$c_g = c_{g,0} + \beta_s \tilde{r}_s \Delta c_g, \tag{18}$$

$$\theta = \theta_{g,0} + \beta_n \tilde{r}_n \Delta\theta, \tag{19}$$

where $\Delta c_g = 0.5(\gamma - \gamma^{-1})c_{g,0}$ and $\tilde{r}_s$ and $\tilde{r}_n$ are distances, normalized with $r_{s,\max}$ and $r_{n,\max}$, respectively. To avoid aphysical corrections for trace energy, the normalized distances have been limited to $|\tilde{r}_s| < 2$ and $|\tilde{r}_n| < 3$. Ideally, $\beta_s = \beta_n = 0.5$. Alternatively, these factors can be treated as tuning parameters.

For the present test case, the above algorithm is easily implemented. Fig. 7 shows results after five days for $\beta_0 = 0.01$ and $\beta_s = \beta_n = 0.5$ in panel (a), and for $\beta_0 = 0.05$ and $\beta_s = \beta_n = 0.6$ in panel (b). Even for essentially theoretical settings of the β parameters (Fig. 7(a)), most of the GSE has been removed. For slightly higher values of the β parameters (Fig. 7(b)), the results closely resemble the 'exact' solution of Fig. 1(b).

Computational costs are increased for two reasons. First, the maximum advection velocity of Eq. (18) is increased by a factor

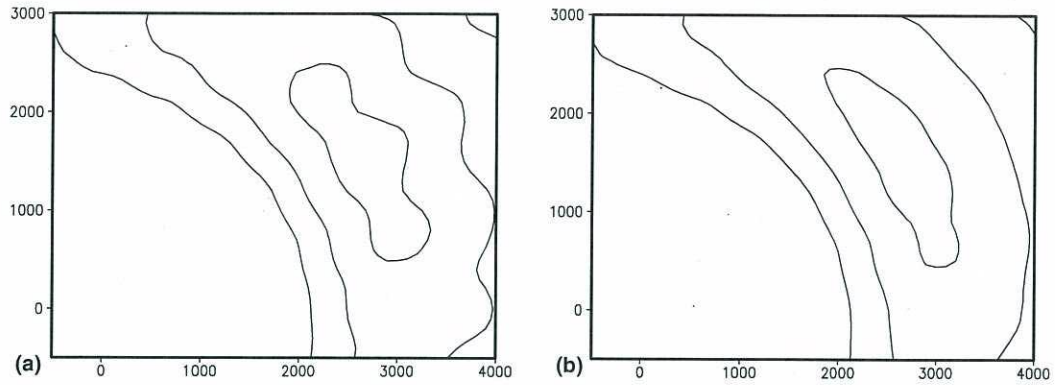

Fig. 7. Like panel (b) of Fig. 1 for UQ scheme with divergent advection and $\beta_0 = 0.01$, $\beta_s = \beta_n = 0.5$ (panel (a)) or $\beta_0 = 0.05$, $\beta_s = \beta_n = 0.6$ (panel (b)).

$$\frac{c_{g,\max}}{c_{g,0}} = 1 + \beta_s(\gamma - \gamma^{-1}) \tag{20}$$

or typically 10–15%. This will require a similar reduction of the numerical time step. Due to the dynamically adjusted time steps for propagation in WAVEWATCH III, and due to the fact that this does not influence the time steps used in the integration of the source terms S on the right side of Eq. (1), the effective increase in computational time of the entire model due to this increased advection velocity is much less, typically of the order of 3–5%.

A second source for increased computational effort is the evaluation of the corrections of the advection velocity. For the present test, this proved simple, because only a single wave field is present for each spectral bin $F(f_i, \theta_j)$. For practical applications, as discussed in the following section, by definition multiple wave fields exist for virtually any $F(f_i, \theta_j)$. For initial testing of this method in practical conditions, a simple generalized algorithm as described in Appendix B has been implemented in WAVEWATCH III.

4. Practical applications

So far, both the importance of, and solutions to the GSE have been discussed in the framework of a highly idealized test case. For practical conditions, the importance of the GSE has been illustrated by Bidlot et al. (1997) and Tolman (2001). Here we will use some practical illustrations to address the capability of different methods to alleviate the GSE.

The GSE is expected to be most prominent in cases with poor spectral resolution, and with strong forcing with small spatial scales. In NCEP's operational models, those with specific hurricane forcing are therefore most sensitive to the GSE. Results of the North Atlantic Hurricane (NAH) model (Chao and Tolman, 2000, 2001; Chao et al., 2001) will therefore be used as an illustration here.

In practical conditions, multiple wave fields generally coexist. The swell field that is most sensitive to the GSE is generally not the major source of local wave energy. The GSE is therefore

rarely obvious in overall significant wave heights H_s. Peak wave periods T_p, defined as the wave period corresponding to the highest value in the local one-dimensional energy spectrum $F(f)$, tend to concentrate more on the dominant swell field. This parameter is therefore a better indicator of the GSE. It is furthermore particularly important, because dominant swells are relevant for offshore operations and safety.

As an example, peak periods T_p of hurricane Alberto from the NAH model are used to examine the GSE effect. In particular, four different model versions have been run to illustrate the occurrence and alleviation of the GSE. The first uses the UQ scheme without GSE alleviation. The second is the standard NAH model, i.e., using an UQ scheme with the BH87 GSE correction and $T_s = 3$ days (computations with $T_s = 1$ day, not influencing time steps, are performed for timing purposes only). The third uses the UQ scheme with the averaging algorithm and $\alpha_s = \alpha_n = 2.00$.

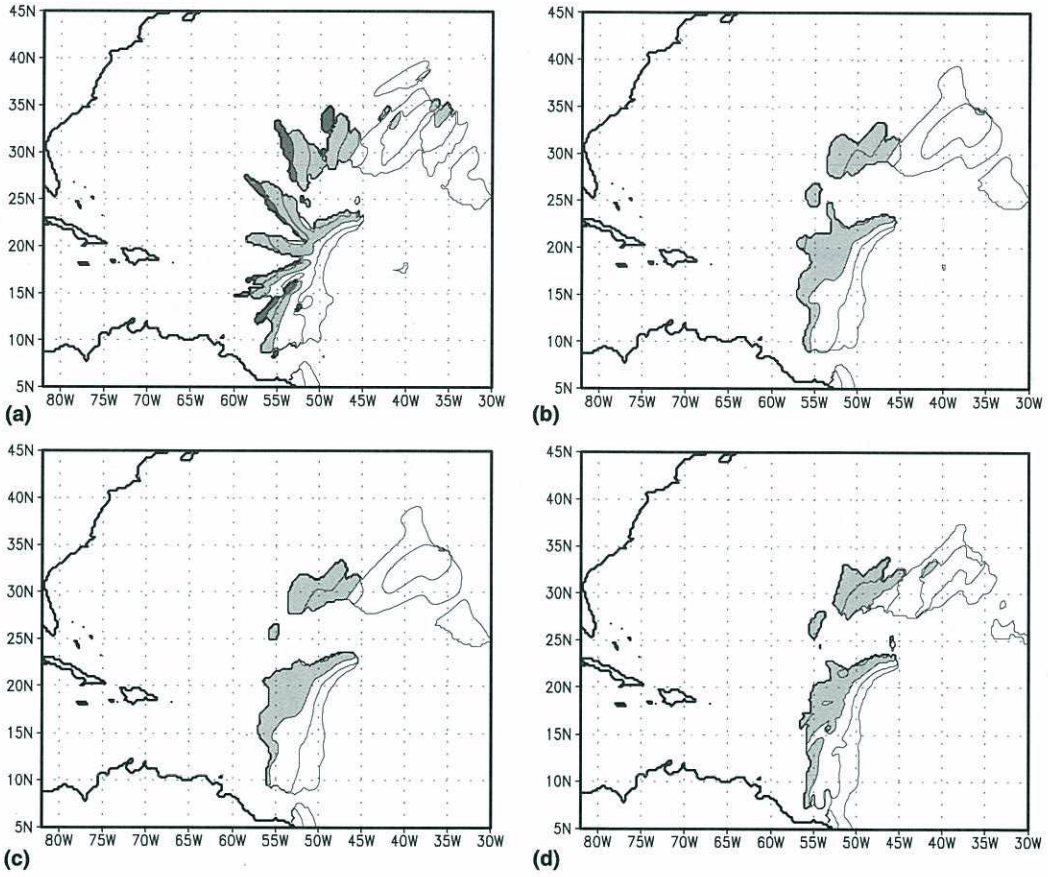

Fig. 8. Peak periods T_p for the swell field generated by hurricane Alberto in NCEP's NAH model for August 9, 2000, 12 GMT. Contours at 1 s intervals starting at $T_p = 9$ s. Light gray shading identifies $11 < T_p < 13$ s, dark gray identifies $T_p > 13$ s. (a) Model with UQ scheme without GSE alleviation. (b) UQ scheme with BH87 diffusion terms and $T_s = 3$ days. (c) UQ scheme with spatial averaging and $\alpha_s = \alpha_n = 2.0$. (d) UQ scheme with divergent advection and $\beta_0 = 0.10$, $\beta_s = 0.50$, and $\beta_n = 0.75$.

The final model version uses the UQ scheme with the divergent advection and $\beta_0 = 0.10$, $\beta_s = 0.50$, $\beta_n = 0.75$. Considering Eq. (20) and the choice of β_s, the maximum propagation time step was reduced by 10%. An additional example from the same model runs for hurricane Florence can be found in Tolman (2001).

Alberto roamed the North Atlantic from August 4–23, 2000. On August 6, Alberto intensified around 15°N and 35°W, and started sending out a distinct swell field. The swell field becomes apparent in the peak periods T_p on August 7, and remains a distinct feature of the peak period fields for the next 4–5 days. It started displaying the GSE in the plain UQ version of the model on August 8. On August 9, the GSE is well developed as is illustrated in Fig. 8(a). Clearly visible are the 'spokes' of large periods, radiating out from roughly 15°N and 35°W.

Normal dispersion along these spokes would show longer waves (larger T_p) lead shorter waves, with contours perpendicular to the propagation direction. Instead, in these spokes, areas with given T_p appear systematically rotated in Fig. 8(a). This is most likely due to an interaction between the GSE and a change of direction of waves following great circles rather than straight lines. This behavior should therefore be considered an additional numerical propagation error related to the GSE.

The wave field in Fig. 8(a) is more complex than the wave field in the previous test, because it consists of many swell fields. For instance, around 22°N and 47°W another swell field can be observed that does not display signs of the GSE. Furthermore, it should be noted that the T_p field by definition is discontinuous, as the instantaneous peak of the spectrum is displayed. 'Holes' in a field of peak periods are therefore not necessarily representing holes in the underlying swell field. Instead, they show an area where other parts of the spectrum become dominant. For instance, between the clear GSE wave field and the US east coast, local wind seas and lesser swell fields are dominating T_p. To isolate the hurricane swells and obtain a clearer picture, such fields are suppressed in the figure by not showing contours for $T_p < 9$ s.

All three GSE alleviation methods used (Figs. 8(b)–(d)) appear to remove the GSE effectively. The smoothest solutions are obtained by the BH87 method (Fig. 8(b)), and the averaging method (Fig. 8(c)), which yield nearly identical results. The most detailed solution is obtained by the divergence method (Fig. 8(d)). Since no exact solution is available, and since all three methods have removed the GSE adequately, it is impossible to identify which method is the best one.

The results of Fig. 8 are fairly representative for the entire two month period considered here. A qualitatively similar example for hurricane Florence is shown in Tolman (2001, Fig. 2). Nevertheless some remnants of the GSE appear to occur in isolated cases. The most pronounced residual GSE for the two month period considered here occurred for the above swell field from Al-berto around August 11. The corresponding results for 00 GMT are presented in Fig. 9. Although most of the GSE, as is evident in panel (a), has been removed by all methods, some residual GSE appears evident for all methods (panels (b)–(d)), particularly between 33°N and 37°N, and 45°W and 60°W.

The main reasons to search for alternative GSE alleviation methods is to find cheaper methods for high resolution models. Table 1 therefore presents relative computational costs (wallclock times) for several methods. All costs are normalized with the run time for the UQ model without GSE alleviation. All runs were performed on a four processor 700 MHz Intel Zeon machine running Red Hat Linux 6.2 and using a Portland Group compiler. The OpenMP version of WAVEWATCH III was run on all processors for the full months of August and September 2000, in four day segments. Average values for the entire two month period are presented in Table 1.

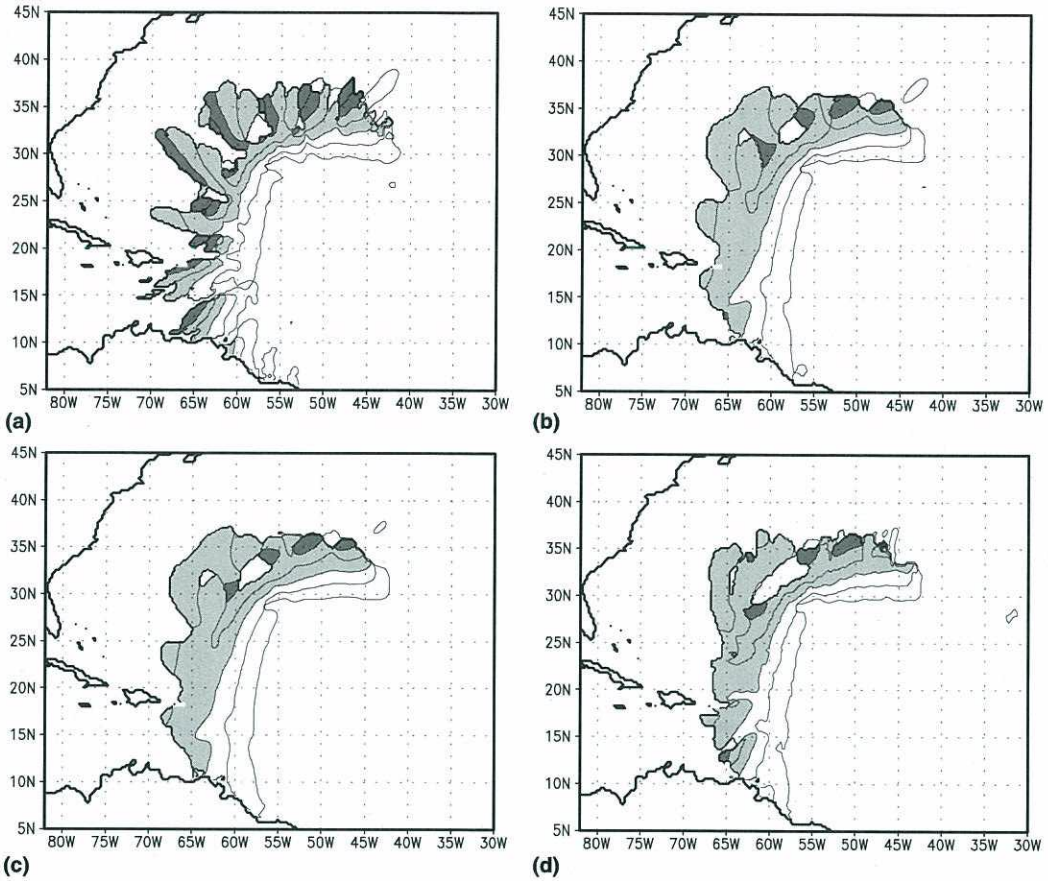

Fig. 9. Like Fig. 8 for August 11, 2000, 00 GMT.

Table 1
Relative run times of NAH models with UQ scheme with different GSE alleviation methods

Plain UQ	UQ/BH87 with $T_s = 1$ day	UQ/BH87 with $T_s = 3$ days	UQ with averaging	UQ with divergence
1	1.15	1.74	1.11	1.69

Timing results for individual four day segments showed no noticeable variability, except for the divergence method.

Timing results for the UQ scheme with the BH87 GSE alleviation method have already been discussed in Section 1. The BH87 diffusion operator by itself adds 15% to the computational time of the model. Proper choice of $T_s \approx 3$ days, however, reduces the attainable time step for propagation, and hence increases the computational time by 74%. The averaging method increases the computational costs of the model by 11%. This method is therefore always cheaper than the BH87 diffusion operator, even if the latter method does not dictate numerical time steps. The divergent advection velocity method, as implemented here, leads to a sizeable increase of computational

time of 69%. Note that the computational costs of this method critically depend on the filter settings as discussed in Appendix B.

5. Discussion

The GSE is a potentially serious problem in ocean wave models. The solution suggested by BH87, which adds a diffusion tensor to the propagation equation, appears to work satisfactorily. It is, however, rather expensive for models with high spatial resolution, due to inherent constraints on numerical time steps. In the present paper, alternatives are investigated, mainly to improve numerical economy. Two alternatives are presented. One adds a spatial averaging step to the equation. The other adds controlled divergence to the advection vectors.

The averaging technique as presented in Section 2 and Appendix A is similar to the diffusion technique of BH87, since the spatial orientation of the averaging area mimics the diffusion tensor. The main advantage of the averaging technique over the BH87 diffusion approach is that it is cheaper in all cases, but particularly for high resolution models, because it has no impact on the propagation time step of the model. An undesirable aspect of the BH87 method is that it requires application specific tuning of T_s. For instance, if the idealized test case used here is extended to 10 days on an appropriately enlarged grid, T_s needs to be increased similarly to suppress the GSE after 10 days. Unfortunately, the averaging technique shares this problem; in an extended test, α_s and α_n need to be increased significantly to remove the GSE after 10 days (figures not presented here).

The technique using a divergent advection velocity is different from the diffusion or averaging technique for three main reasons: (i) The diffusion and averaging techniques are applied locally to a spatial bin, whereas the divergence method is applied globally to a contiguous swell field. This implies that the local spreading applied in the divergence technique per spatial grid point scales with $(\Delta c_g, \Delta\theta)/N$, where N is the spatial extent of the swell field in terms of grid increments Δx. This implies that the *local* spreading applied in the divergence method is typically a factor $1/N$ smaller than with the other two methods. (ii) The divergence method is inherently two-dimensional, generating crescent shaped discrete swell fields, whereas the other two methods only spread wave energy along the propagation and perpendicular directions. (iii) The divergence method with near-ideal settings performs just as well after 10 days in the idealized test as after 5 days (figures not presented). Hence, this method is not expected to require much application dependent tuning, unlike the other two methods.

The three GSE alleviation methods with parameter settings as in Figs. 2(b), 5(b) and 7(a) give for practical purposes identical results in the idealized test case. To further assess differences in the inner workings of the three methods, a modified idealized test case has been run for these model settings. In this test, all initial wave energy is concentrated in the dominant spectral bin only ($\theta_m = 30°$, $f_m = 0.1$ Hz). Fig. 10 shows the corresponding significant wave height (H_s) distributions in 1 day intervals, with contours at 20% intervals of the instantaneous maximum H_s. Also shown in the figure are the expected data envelopes in the case of no spectral dispersion (dotted lines), and of a directional dispersion of $\pm 0.5\Delta\theta$ (dashed lines). These lines are offset by 400 km from the initial maximum wave height, to nearly touch the initial 20% H_s contour.

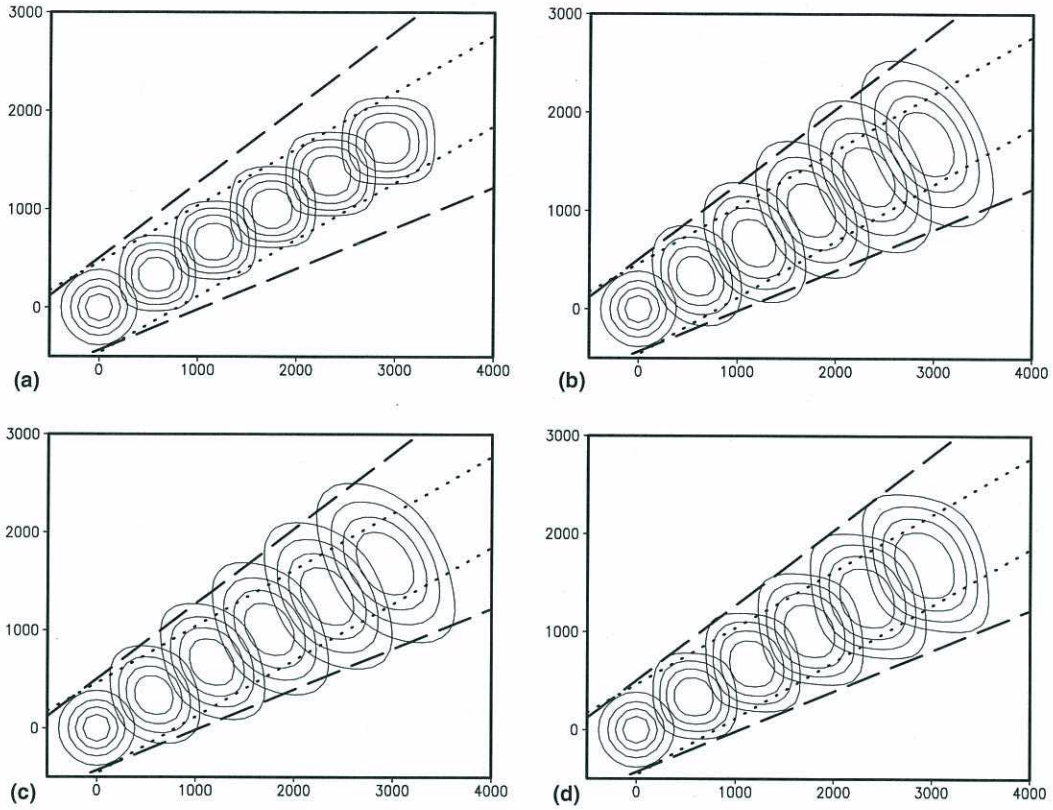

Fig. 10. Modified idealized test case with one energy containing spectral bin ($\theta_m = 30°$, $\Delta\theta = 15°$, $f_m = 0.1$ Hz, $\gamma = 1.1$). Contours at 20% intervals of instantaneous maximum significant wave height H_s for initial conditions, and at 1 day intervals up to five days. Dotted lines: expected data envelope without spectral sub-grid dispersion. Dashed line: expected data envelope for energy evenly distributed over $\Delta\theta$. (a) UQ scheme, (b) UQ and BH87 as in Figs. 2(b), (c) UQ and averaging as in Fig. 5(b), (d) UQ and divergence as in Fig. 7(a).

The plain UQ scheme (Fig. 10(a)) is expected to advect the initial distribution without changing its shape, i.e., staying tightly within the dotted lines. Changes in the shape of the wave height distribution indicate well documented numerical errors of the UQ scheme. Mostly however, nondispersive advection is accurately modelled, and numerical errors appear negligible compared to the expected directional dispersion (dashed lines).

The UQ scheme with the BH87 diffusion method or the present averaging method (Figs. 10(b) and (c)) again show virtually identical results. Based on the lowest (20%) wave height contours, and the expected dispersion envelopes at $\pm 0.5\Delta\theta$ (dashed lines), both schemes are too aggressive in spatially spreading the energy in a single spectral bin. In spite of this, the entire wave field (Figs. 2(b) and 5(b)) still shows remnants of the GSE. Note that the 'theoretical' setting for the tunable parameters in both models ($T_s \approx 2.5$ days for BH87, $\alpha_s = \alpha_n = 0.5$ for averaging), are much smaller than the values used in obtaining the results of Figs. 2(b), 5(b) and 10(b)–(c). Without further analysis, this might have suggested that swell fields for individual spectral bins need to be

excessively smoothed to get good model results for the entire spectrum. Figs. 10(b)–(c) show that the schemes in fact are only moderately too aggressive in smoothing individual wave fields.

The UQ scheme with divergent advection (Fig. 10(d)) and with the 'theoretical' settings $\beta_0 = 0.01$ and $\beta_s = \beta_n = 0.5$ shows near ideal directional dispersion at the 20% contour level (compare lowest contour with dashed line), and here does not display the overly smoothed behavior of the previous two schemes. At the 80% level (highest contour levels), the dispersion of the wave heights is nearly identical to that of the other two methods. This explains why the divergence method yields nearly identical results for the overall wave field in Fig. 7, while needing less smoothing of the individual wave fields in Fig. 10. This identifies a fourth difference between the divergence and other methods; the linear directional dispersion with $\tilde{r}_n$ in the divergence method is apparently more realistic (or at least more efficient) in removing the GSE, than the inherently nonlinear dispersion due to diffusion or averaging. Note that the two-dimensional structure of the divergent correction is not obvious here for the relatively small directional increment. For larger directional increments (figures not presented here), it becomes obvious.

The above differences explain a paradox in the results of different methods for either the idealized or real world cases presented. In the idealized test case (Figs. 1, 2, 5 and 7) the divergence method gives similarly smooth or smoother results. In the real work case, however, (Figs. 8 and 9) the same method gives less smooth results. This is possibly due to the somewhat excessive smoothing needed in the BH87 or averaging methods needed to remove the GSE for individual swell fields. This is bound to lead to similarly excessive smoothing of the overall wave fields. The fact that the divergence method needs less local smoothing for individual wave fields may well explain why overall wave fields also appear less smooth. It should, however, again be stressed that a lack of an 'exact' solution in the real world cases makes it impossible to define which method is the most accurate.

This study was started to find a cheaper GSE solution than the BH87 diffusion operator for models with high spatial resolution. The new averaging technique presented here appears to offer an ideal choice. Its results are virtually identical to those of the BH87 approach. For large scale models, such as NCEP's global model, the reduction in model run time compared to the BH87 method is moderate (4% for the equipment used here). For small scale models, particularly the North Atlantic Hurricane model, the reduction in model run time is expected to be significant (30% for the equipment used here).

From a theoretical perspective, and based on idealized test cases, the divergent advection method suggested here appears superior to the other two GSE alleviation methods. In its present form, however, it is much more expensive than the averaging method for practical applications. Considering the small differences in model results, such an increased expense does not seem justifiable in operational models.

In its present form, the costs of the divergence method critically depend on the decomposition of wave fields for a given spectral bin into individual wave fields. Its economy can be influenced dramatically by modifying the different filter levels as discussed in Appendix B. However, the expensive nature of this method is a direct consequence of the decomposition method used here. Any such method will require linear search elements, which are notoriously inefficient. It is unlikely that any method requiring such a decomposition will be able to rival the economy of the averaging technique. For this reason, further attempts to find cheaper instantaneous decomposition methods have been abandoned.

An alternative has already been identified in Section 3 in using separate evolution equations for the location and extent of swell fields. In such a case, search algorithms are only needed in wave generation areas, whereas for established swell fields, corrections for the advection vector can be established with minimal effort. However, developing such a set of parallel equations, particularly for spherical grids where the direction of swell changes along their great circle paths, is far from trivial. However, because the divergence method appears to have some physical advantages, and particularly has the potential to allow for GSE alleviation without removing shadow zones behind islands, it does appear to be a candidate for additional research.

6. Conclusions

The GSE is a potentially serious problem in ocean wave models. A solution to this problem has been suggested by Booij and Holthuijsen (1987, BH87). Whereas this method works satisfactorily, it also adds significant computational effort to high resolution models. This increase is mostly due to the fact that the diffusion terms introduced in this technique adversely influence numerical time steps. In the present paper a new averaging technique is introduced. Its results are nearly identical to the BH87 techniques, yet have no impact on numerical time steps. This method is therefore significantly cheaper for high resolution models. A second alternative method adds divergence to the advection field. This method appears superior from a physical perspective, and unlike the other methods does not appear to need application specific tuning. However, it is presently too expensive for operational models. Some suggestions are made for further research into the latter method.

Acknowledgements

The author would like to thank Larry Burroughs, Y.Y. Chao, D.B. Rao, Weixing Lin, Naomi Surgi, and the anonymous reviewers for their comments on early drafts of this paper. The present study was partially supported by funding from the NOAA High Performance Computing and Communication (HPCC) office.

Appendix A. Spatial averaging

Let the vectors $\vec{s}$ and $\vec{n}$ in (x,y)-space define the extent of the averaging area in Fig. 4 and Eq. (15) in the propagation and normal direction, respectively. Normalized with the grid steps, they are given as

$$\vec{s} = \begin{pmatrix} 0.5\alpha_s(\gamma - \gamma^{-1})c_g\Delta t\cos(\theta)(\Delta x)^{-1} \\ 0.5\alpha_s(\gamma - \gamma^{-1})c_g\Delta t\sin(\theta)(\Delta y)^{-1} \end{pmatrix}, \tag{A.1}$$

$$\vec{n} = \begin{pmatrix} -\alpha_n\Delta\theta c_g\Delta t\sin(\theta)(\Delta x)^{-1} \\ \alpha_n\Delta\theta c_g\Delta t\cos(\theta)(\Delta y)^{-1} \end{pmatrix}. \tag{A.2}$$

The four vectors $\vec{r}_{1,2,3,4}$ defining the corners of the interpolation area in counterclockwise direction then become

$$\begin{aligned}\vec{r}_1 &= \vec{s} + \vec{n},\\ \vec{r}_2 &= -\vec{s} + \vec{n},\\ \vec{r}_3 &= -\vec{s} - \vec{n},\\ \vec{r}_4 &= \vec{s} - \vec{n},\end{aligned} \tag{A.3}$$

where the origin of $\vec{r}$ is at the grid point considered. In obtaining the values at the gray points in Fig. 4, one of the outer corners of the nine-point stencil is always involved. This point is easily found from the signs on the components of the vectors $\vec{r}$. The adjacent point for interpolation then is found by comparing the absolute values of the components of the vector. The interpolation weight factor for the corner point of the stencil then becomes

$$\frac{\min(|r_{\mathrm{n},x}|, r_{\mathrm{n},y}|)}{\max(|r_{\mathrm{n},x}|, r_{\mathrm{n},y}|)}, \tag{A.4}$$

where $r_{\mathrm{n},x}$ and $r_{\mathrm{n},y}$ are the x and y components of the four vectors $\vec{r}_{\mathrm{n}}$. With this weight factor, the intermediate spectral densities at the gray points in Fig. 4 are defined. The weight for the gray point in the averaging along the dashed lines in Fig. 4 is given as the absolute value of the proper component of the vector $\vec{r}_{\mathrm{n}}$. Finally, using the average of the means of four triangles spanned by the central points and two adjacent $\vec{r}_{\mathrm{n}}$, the average value F_{avg} is estimated as

$$F_{\mathrm{avg}} = \frac{1}{6}\sum_{n=1}^{4} F(\vec{r}_{\mathrm{n}}) + \frac{1}{3}F(\vec{r}=0). \tag{A.5}$$

The global energy conservation of this scheme needs to be assured, so that the averaging does not create or dissipate energy. The above averaging scheme can be rewritten in the form

$$F_{\mathrm{avg}}(f_i,\theta_j;x_l,y_m) = \sum_{L=-1}^{1}\sum_{M=-1}^{1} a_{L,M}(x_l,y_m)F(f_i,\theta_j;x_{l+L},y_{m+M}), \tag{A.6}$$

where l and m are absolute discrete grid counters in physical space, and L and M are corresponding relative counters. Thus, for each (x_l, y_m), the original spectral density $F(x_l, y_m)$ contributes to nine surrounding averaged spectral densities $F_{\mathrm{avg}}(x_l, y_m)$. Global conservation requires that the sum of all corresponding factors a applied to $F(x_l, y_m)$ equals 1, or

$$\sum_{L=-1}^{1}\sum_{M=-1}^{1} a_{L,M}(x_{l-L},y_{m-M}) = 1. \tag{A.7}$$

For a given spatial point (x_l, y_m) and spectral bin (f_i, θ_j), Eq. (A.1) shows that $\vec{s}$ and $\vec{n}$, and hence the coefficients $a_{L,M}$ are a function of c_{g}, γ, $\Delta\theta$, Δt, Δx and Δy. By definition, Δt is constant for a wave field. For most models, the same is true for γ and $\Delta\theta$. For the present test case, grid increments Δx and Δy are constant across the grid, and the deep water conditions make c_{g} constant as well. Hence, $a_{L,M}$ are constant across the spatial grid, and because

$$\sum_{L=-1}^{1}\sum_{M=-1}^{1} a_{L,M}(x_l, y_m) \equiv 1, \tag{A.8}$$

the interpolation method is conservative. However, for shallow-water applications, where c_g varies across the grid, or for spherical grids, where Δx varies with y, $a_{L,M}$ varies across the grid and Eq. (A.7) will generally not hold. Hence in such conditions the above averaging scheme is not conservative. A simple solution to obtain a conservative averaging, is to use $a_{L,M}(x_l, y_m)$ to distribute the energy $F(x_l, y_m)$, rather than to gather the energies from the nine-point stencil. This replaces Eq. (A.6) with

$$F_{\mathrm{avg}}(x_l, y_m) = \sum_{L=-1}^{1}\sum_{M=-1}^{1} a_{L,M}(x_{l-L}, y_{m-M}) F(x_{l-L}, y_{m-M}) \tag{A.9}$$

dropping the dependence of F on (f_i, θ_j) for brevity. For this averaging scheme to be conservative, only (A.8) needs to be satisfied, which is the case by definition. Note that this final averaging scheme is identical to (A.6) for constant c_g, Δx and Δy (as in the idealized test case). Finally, to avoid excessive 'bleeding' of energy into coastlines parallel to the x or y axes, energy is not distributed onto land.

Appendix B. Divergent advection

The method for correcting the advection velocity and direction as outlined in Section 3 is easily implemented for a test case where only one discrete swell field is present for each $F(f_i, \theta_j)$. In practical conditions multiple fields are present and an iterative method is required. A simple iterative method is to find all local maxima, and to identify swell fields by descent methods from those maxima. Eqs. (17)–(19) then can be applied to each such field individually.

A first implementation of such a scheme in WAVEWATCH III was found to be prohibitively expensive for practical applications. To reduce the computational time needed, some filtering is introduced. The first is an absolute filter, stating that only bins with an equivalent wave height less than H_{min} will be considered in the search for individual fields, i.e.,

$$F > \frac{H_{\mathrm{min}}^2}{16\Delta f_r \Delta\theta_r}, \tag{B.1}$$

where $\Delta f_r = 0.1f$ and $\Delta\theta_r = 15°$ are representative rather than actual grid spacings, to avoid sensitivity of filtering to the spectral resolution. Similarly, a relative filtering is applied, using only spectral densities that are larger than a fraction ϵ times the global maximum spectral density F_{max} for the spectral bin (f_i, θ_j)

$$F > \epsilon F_{\mathrm{max}}. \tag{B.2}$$

Even though this filtering significantly reduces the computational costs of the search algorithm, resulting run time still are prohibitive. This is easily explained because literally hundreds of

individual fields were found for many spectral bins. Because many of such fields are essentially 'noise', the last filter applied was to only apply the correction for the first N_{max} fields found for each spectral bin. The practical results obtained with WAVEWATCH III as presented in Section 4 are obtained with $H_{min} = 0.001$ m, $\epsilon = 0.001$ and $N_{max} = 25$.

References

Bidlot, J.R., Janssen, P., Hansen, B., Guenther, H., 1997. A modified set up of the advection scheme in the ECMWF wave model. Technical memorandum 237, ECMWF, 31 pp.

Booij, N., Holthuijsen, L.H., 1987. Propagation of ocean waves in discrete spectral wave models. Journal of Computational Physics 68, 307–326.

Booij, N., Ris, R.C., Holthuijsen, L.H., 1999. A third-generation wave model for coastal regions, Part I, model description and validation. Journal of Geophysical Research 104, 7649–7666.

Chao, Y.Y., Burroughs, L.D., Tolman, H.L., 2001. The North Atlantic Hurricane wind wave forecasting systems. Technical Procedures Bulletin 478, NOAA/NWS, online [1].

Chao, Y.Y., Tolman, H.L., 2000. Numerical experiments on predicting hurricane generated wind waves. In: Sixth International Workshop on Wave Hindcasting and Forecasting (preprints). Environment Canada, pp. 167–179.

Chao, Y.Y., Tolman, H.L., 2001. Specification of hurricane wind fields for ocean wave prediction. In: Edge, B.L., Hemsley, J.M. (Eds.), Ocean Wave Measurements and Analysis. ASCE, pp. 671–679.

Chen, H.S., Burroughs, L.D., Tolman, H.L., 1999. Ocean surface waves. Technical Procedures Bulletin 453, NOAA/NWS, online [2].

Hasselmann, S., Hasselmann, K., Allender, J.H., Barnett, T.P., 1985. Computations and parameterizations of the nonlinear energy transfer in a gravity-wave spectrum, Part II: parameterizations of the nonlinear energy transfer for application in wave models. Journal of Physical Oceanography 15, 1378–1391.

Komen, G.J., Cavaleri, L., Donelan, M., Hasselmann, K., Hasselmann, S., Janssen, P.E.A.M., 1994. Dynamics and Modelling of Ocean Waves. Cambridge University Press, Cambridge, 532 pp.

Lavrenov, I.V., Onvlee, J.R.A., 1995. A comparison between the results of wave energy propagation of the WAM model and the interpolation-ray method. Russian Meteorology and Hydrology 3, 29–42.

Leonard, B.P., 1979. A stable and accurate convective modelling procedure based on quadratic upstream interpolation. Computational Methods in Applied Mechanical Engineering 18, 59–98.

Leonard, B.P., 1991. The ULTIMATE conservative difference scheme applied to unsteady one-dimensional advection. Computational Methods in Applied Mechanical Engineering 88, 17–74.

Ris, R.C., Holthuijsen, L.H., Booij, N., 1999. A third-generation wave model for coastal regions, Part II: verification. Journal of Geophysical Research 104, 7667–7681.

Snodgrass, F.E., Groves, G.W., Hasselmann, K.F., Miller, G.R., Munk, W.H., Powers, W., 1966. Propagation of swell across the pacific. Transactions of the Royal Society of London, A 259, 431–497.

Tolman, H.L., 1992. Effects of numerics on the physics in a third-generation wind-wave model. Journal of Physical Oceanography 22, 1095–1111.

Tolman, H.L., 1995. On the selection of propagation schemes for a spectral wind wave model. Office Note 411, NWS/NCEP, 30 pp + figures.

Tolman, H.L., 1999. User manual and system documentation of WAVEWATCH III version 1.18. Tech. Note 166, NOAA/NWS/NCEP/OMB, 110 pp.

Tolman, H.L., 2001. Improving propagation in ocean wave models. In: Edge, B.L., Hemsley, J.M. (Eds.), Ocean Wave Measurements and Analysis. ASCE, pp. 507–516.

[1] http://polar.wwb.noaa.gov/omb/tpbs/nah_tpb/tpb_nah_txt.htm

[2] http://polar.wwb.noaa.gov/omb/tpbs/nww3tpb/nww3tpb.html

Tolman, H.L., Chalikov, D.V., 1996. Source terms in a third-generation wind-wave model. Journal of Physical Oceanography 26, 2497–2518.

WAMDIG, 1988. The WAM model – a third generation ocean wave prediction model. Journal of Physical Oceanography 18, 1775–1809.